Corrosion Science 245 (2025) 112711

Contents lists available at ScienceDirect

Corrosion Science

journal homepage: www.elsevier.com/locate/corsci

Fatigue and corrosion fatigue performance of selective laser melted AlSi10Mg and die cast A360 aluminum alloys

Hongqian Chen [a], Peng Liu [a], Xuechong Ren [a,*], Alex A. Volinsky [b]

[a] National Center for Materials Service Safety, University of Science and Technology Beijing, Beijing, 100083, PR China
[b] Department of Mechanical Engineering, University of South Florida, 4202 E. Fowler Ave. ENG030, Tampa 33620, USA

ARTICLE INFO

Keywords:
AlSi10Mg
Corrosion fatigue
Lack of fusion defects
Pits

ABSTRACT

The fatigue performance of selective laser melting (SLM) AlSi10Mg and die-cast A360 alloys was studied in air and 0.6 M (3.5 wt%) NaCl solution. The SLMed-AlSi10Mg exhibits lower *S-N* data compared to the A360 alloy in both environments, despite having higher strength and ductility. Lack of fusion defects and cyclic slip serve as fatigue initiators for SLMed-AlSi10Mg and A360 alloy in air, respectively. In the 0.6 M NaCl solution, the *S-N* data of both alloys significantly decrease compared to the air environment. No fatigue limit was observed as the fatigue lives sustain to increase beyond 10^7 cycles. Pitting acts as the fatigue initiator at low stress levels ($S_{max} <$ 100 MPa), while the failure mechanism at high stress levels ($S_{max} >$ 120 MPa) remains consistent with that in air. Prior corrosion for 72 hours in the 0.6 M NaCl solution results in only a negligible decrease in fatigue performance of both alloys. Electrochemical analysis indicates that SLMed-AlSi10Mg has higher pitting sensitivity but a lower uniform corrosion rate due to its microstructure homogeneity. The combined effects of pitting sensitivity and corrosion rate result in similar corrosion fatigue sensitivity of both alloys. Additionally, the *S-N* data of SLMed-AlSi10Mg shows large dispersion and a small Weibull shape parameter due to variations in defect sizes and different pitting morphology.

1. Introduction

Additive manufacturing (AM) has increasingly gained popularity in the design and formation of complex shapes [1,2] for its incremental building strategy based on computer-aided design (CAD) models. The main advantages of AM include reduced material processing costs and the ability to produce customized designs with high strength-to-weight ratios through topology optimization [3,4]. Selective laser melting (SLM), a type of powder bed fusion (PBF) technology that uses laser as a heat source and scans the powder layer by layer along a tool path determined by sliced CAD data, has been successfully employed to fabricate various metal parts.

AlSi10Mg is widely used in the aviation and automotive industries due to its low density and high strength-to-weight ratio. Its hypoeutectic composition provides good fluidity and low solidification shrinkage, making it well-suited to be formed by SLM technology. The rapid solidification process in SLM results in a microstructure for AlSi10Mg that consists of very fine cells and Al-Si eutectic networks [5,6]. The fine structure makes it exhibit higher strength and ductility compared to cast parts. However, defects such as gas pores, lack of fusion (LOF) pores, and surface roughness [7,8] are detrimental to fatigue performance. Numerous studies have focused on the benefits of heat treatment [9,10] and surface strengthening [11,12] on the fatigue performance of SLMed-AlSi10Mg. Brandl *et al.* [9] found that T6 treatment could improve its fatigue performance, while Zhang *et al.* [10] observed that the as-produced state showed the best fatigue performance, potentially due to differences in stress ratio and processing parameters. On the other hand, quality control of AM components should consider the quantitative analysis of defect sizes [13,14].

However, for aluminum alloys corrosion must also be considered in fatigue assessments because pitting [15–21] and intergranular corrosion [22] could serve as fatigue initiators and lead to premature failure when exposed to moist air, rainwater, or seawater environment. Corrosion fatigue (CF) is a material failure process driven by the synergistic effects of cyclic stress and a corrosive environment. Lin *et al.* [16] found that the conditional fatigue limits of T73 and T6 tempered 7050 alloys decreased by 67.4 % and 37.5 % in a 3.5 wt% NaCl solution, respectively. The higher CF sensitivity of the T73 temper was attributed to greater pitting density induced by larger precipitate size and spacing. Sharma *et al.* [18] reported that ultrafine-grained Al-7.5Mg alloy possessed higher CF

---

* Corresponding author.
E-mail address: xcren@ustb.edu.cn (X. Ren).

https://doi.org/10.1016/j.corsci.2025.112711
Received 19 October 2024; Received in revised form 12 January 2025; Accepted 13 January 2025
Available online 15 January 2025

sensitivity than 5083 alloy due to deeper intergranular corrosion pits, though the latter showed a more severe corrosion damage.

Prior corrosion can also be as harmful as synergistic CF for some sensitive alloys [23–25]. Guérin *et al.* [23] found that prior corrosion for 72 hours in T84 Al-Cu-Li alloy is more detrimental to the fatigue performance relative to synergistic CF. In contrast, prior corrosion for shorter times would lead to the same decrease in fatigue life as synergistic CF with same duration, indicating a weak mutual interaction between cyclic stress and corrosion.

Behvar *et al.* [26] suggested that hydrogen blistering might be more likely in additive materials due to their numerous internal and surface defects. For SLMed-AlSi10Mg, pitting corrosion can occur in a selective corrosion of the Al matrix manner due to the different electrochemical potentials between Al cells and Si networks [27,28]. However, there are very limited studies on the corrosion fatigue performance of SLMed-AlSi10Mg, which may exhibit different failure mechanisms compared to traditional castings [29,30]. Leon *et al.* [29] reported that the low-cycle (3 % strain amplitude) bending fatigue life of SLMed-AlSi10Mg reduced by about 20 % in a 3.5 wt% NaCl solution, which was attributed to pitting corrosion. Linder *et al.* [30] found that combined atmospheric corrosion and fatigue could reduce fatigue life more with respect to prior corrosion especially at low stress levels for SLMed-AlSi10Mg. Processing defects and stress concentration at the corners of rectangular specimens were identified as the primary origin of main cracks. However, secondary cracks was observed initiated from pits.

The main objective of this study is to investigate the effects of prior corrosion and synergistic CF on the fatigue performance of SLMed-AlSi10Mg and A360 alloys with nearly identical compositions. Failure mechanisms were identified by analyzing fracture morphologies and comparing microstructures of both alloys. The effects of pitting and lack of fusion defects on the fatigue crack initiation process were discussed. Electrochemical tests were conducted to understand the relationship between microstructure, corrosion behavior, and CF sensitivity. The dispersion of *S-N* data was analyzed through statistical analysis of critical defect sizes and Weibull shape parameters.

2. Experiment

2.1. Materials

Rod-like AlSi10Mg specimens were produced by Xi'an Bright Laser Technologies Co., Ltd. Schematics of the SLM process is shown in Fig. 1(a), along with the produced samples in Fig. 1(b). The composition of the AlSi10Mg powder is listed in Table 1. The powder size ranged from 15 μm to 45 μm. An IPG 500 W laser with a beam diameter of 80 μm was used as the energy source. Optimized processing parameters were adopted and listed in Table 2. All specimens were printed vertically with the axial line parallel to forming direction. After the 3D-printing process, all specimens were subjected to heat treatment at 280 °C for 2 hours to relieve residual stress corresponding to the SR1 conditions in ASTM 3318–18 [31].

Table 1
Chemical composition (wt%) of the AlSi10Mg powders and A360 alloy.

Material	Si	Mg	Mn	Fe	O	Al
SLMed-AlSi10Mg	9.71	0.41	0.025	0.096	0.037	Bal.
A360 alloy	9.84	0.42	0.33	0.8	-	Bal.

For A360 die-cast aluminum alloy, several rods with a 12 mm diameter and a 10 mm thick plate were cut from a $150 \times 150 \times 150$ mm^3 cube. The T6 heat treatment was applied for structural homogenization which involved a solution treatment at 535 °C for 4 hours followed by water quenching, aging at 175 °C for 4 hours and air cooling. The composition of the A360 alloy was also listed in Table 1.

Several $10 \times 10 \times 10$ mm^3 cubes were cut from SLMed-AlSi10Mg specimens and A360 plate for microstructure characterization. The surfaces were ground using 240, 600, 1000, and 2000 grit sandpaper, and then polished with 1 μm diamond paste and 50 nm SiO_2 suspension. After etching with Keller's reagent the microstructure was observed using optical microscopy.

Tensile tests were conducted on an MTS 100 kN testing machine using small-size specimens (D = 6 mm, G = 30 mm) which conformed to ASTM E8M-22 [32]. Each tensile test was repeated three times. Vickers hardness $Hv_{0.2}$ was measured using a Qness hardness tester. The hardness values were averaged from five measurements taken 1 mm apart along a line.

2.2. Electrochemical tests

Table 2
Selective laser melting process parameters.

Laser power	Scan speed	Hatch space	Layer thickness	Pattern	Rotation angle
400 W	1700 mm/s	0.17 mm	30 μm	Zig-zag	67°

Several $10 \times 10 \times 10$ mm^3 cubes were cut from the grips of the

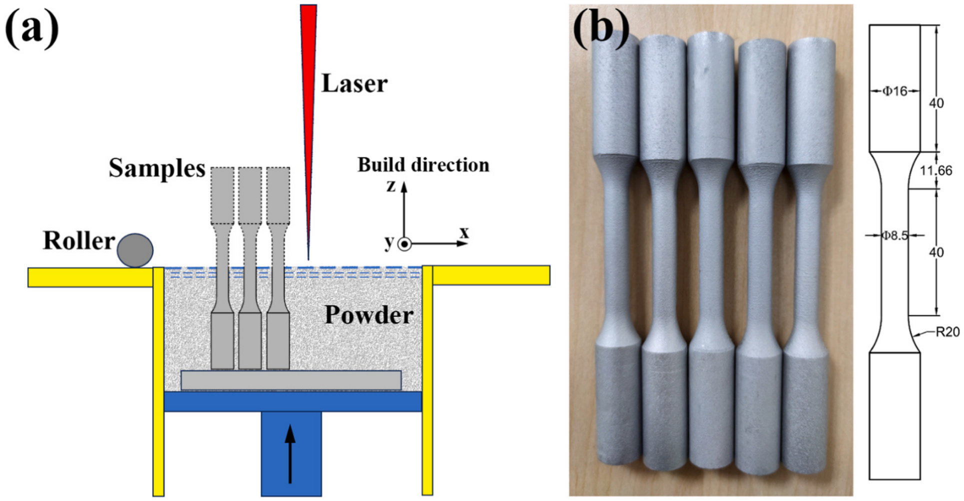

Fig. 1. (a) Schematics of the selective laser melting process and (b) as-processed specimens. Here, dimensions are in mm.

fatigue specimens for SLMed-AlSi10Mg samples, and from the plate after T6 treatment for A360 alloy. The cubes were prepared with one exposed surface (x-z plane for SLMed-AlSi10Mg) of 1 cm^2 and the remaining surfaces coated with resin. The test surface was ground by 2000 sandpaper, and then cleaned by deionized water and ethanol.

A three-electrode system was used for the electrochemical tests, with a calomel electrode containing saturated potassium chloride solution as the reference electrode (+0.2438 V *vs.* standard hydrogen electrode (SHE) potential). A 0.6 M NaCl solution was selected as the electrolyte and the tests were conducted at 25 °C. The samples were soaked in the electrolyte for 3600 s to reach a stable open circuit potential (OCP). Then cyclic potentiodynamic polarization (CPDP) curves were measured at a scan rate of 0.1 mV/s from −300 mV (*vs.* OCP). The scan direction was reversed as the current density exceeded 1 mA/cm^2. The test was stopped when −300 mV (*vs.* OCP) was reached. Each test was repeated at least three times to ensure repeatability, and the CPDP curves were analyzed using Versa Studio software. The corrosion potential E_{corr} was taken as the potential where the external measured current was nearly 0. The pit transition potential E_{ptp} was the potential where the change rate of current slowed down abruptly (third derivative equal to 0) in the reversed scan. The repassivation/protective potential E_{prot} is the intersection point of forward scan and reversed scan so it could be obtained from CDPD curve directly.

2.3. Fatigue tests

Fatigue tests were conducted using dog-bone-shaped specimens with a gauge length of 40 mm as shown in Fig. 2(a). The surfaces were carefully ground to achieve a surface roughness R_a of ~0.3 μm. The specimens were divided into four groups: AF-SLM, AF-A360, CF-SLM, and CF-A360. In these designations, "AF" and "CF" represent fatigue testing in air and a corrosive solution environment while "SLM" and "A360" represent the two different materials.

Polystyrene cups were attached to the fatigue specimens using a modified acrylic adhesive and 0.6 M NaCl solution was used as the corrosive medium. Fatigue tests were performed using an MTS 100 kN fatigue testing machine. The tests were conducted with a sine-wave form, using a frequency of 10 Hz in the solution environment and 20 Hz in air. The gauge length of CF specimen was fully immersed in the solution in Fig. 2(b).

To study the effects of prior corrosion on fatigue performance, additional fatigue tests were conducted on a group of specimens that had been pre-corroded in 0.6 M NaCl solution for 72 hours. These groups were designated as PF-SLM and PF-A360. Fatigue tests were terminated either after complete fracture of the specimens or were considered run-out after 10^7 cycles. Corrosion morphology was observed using a laser confocal microscope and a scanning electron microscope (SEM). The fractured surfaces were also examined using SEM.

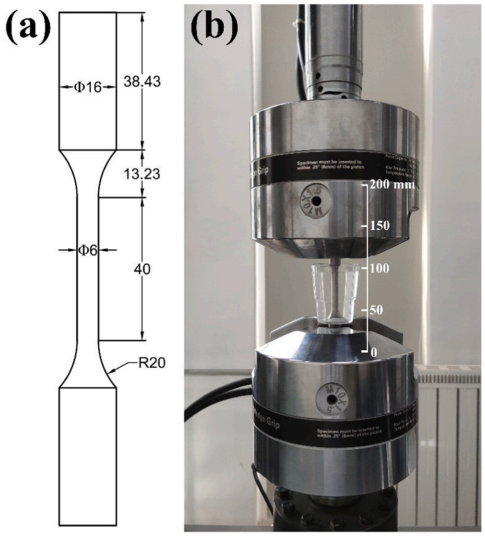

Fig. 2. (a) Fatigue specimens geometry in mm and (b) picture of corrosion fatigue test.

3. Results

3.1. Microstructure and tensile properties

Fig. 3 shows the typical microstructure of SLMed-AlSi10Mg and A360 alloys. For SLMed-AlSi10Mg, the molten pools with characteristic fish scale could be observed in the x-z plane. Coarse Si network was distributed in the boundary and fine homogeneous Si network in the center as shown by Fig. 3(a). The width and height of the molten pools are consistent with the SLM forming parameters in terms of 0.17 mm hatching space and 30 μm layer thickness. The typical non-equilibrium microstructure of additively manufactured materials results from the inhomogeneous distribution of laser energy and the high cooling rate of ~10^6 K/s. In contrast, the A360 alloy exhibits a near-equilibrium structure, characterized by an Al matrix with homogeneous Si particles ranging from 5 μm to 20 μm in diameter as shown by Fig. 3(b).

Stress-strain curves of the SLMed-AlSi10Mg and A360 alloys are shown in Fig. 4. The yield strength (YS), ultimate tensile strength (UTS), and elongation (EL) values are summarized in Table 3. It is evident that the strength and ductility of SLMed-AlSi10Mg are superior to the A360 alloy. This improvement can be attributed to the fine Si network structure considering the fine-grain strengthening. And partial dissolution of Si in the Al matrix could also induce solution strengthening. Wu *et al.* [5] have also proposed that the Si networks and the partial Si in matrix could limit the dislocation movement and hence lead to a high strength.

However, the Vickers hardness of SLMed-AlSi10Mg and A360 alloy is nearly identical which are 103.0 $H_{v0.2}$ and 103.5 $H_{v0.2}$, respectively. The large Si particles in A360 alloy may restrict the local deformation and hence lead to a comparable hardness with SLMed-AlSi10Mg.

3.2. Corrosion behavior

3.2.1. CDPD curves

Fig. 5 shows the cyclic potentiodynamic polarization curves for SLMed-AlSi10Mg and A360 alloys. The corresponding parameters including E_{corr}, E_{ptp} and E_{prot} are summarized in Table 4. On the surface of aluminum alloys there is always a natural oxide film formed in a few milliseconds consisting of an inner amorphous compact layer with a thickness of 2–4 nm [15]. The corrosion behavior is dependent on both the oxide layer and the metal. At the beginning of the CPDP tests, the cathodic current density i_c remains nearly constant over a wide range which indicates a passivation state. When E_{corr} is reached the anodic current density i_a increases dramatically, indicating the local rupture of the passive films and the initiation of pits. Cabrini *et al.* [27] reported that when the NaCl concentration is below 0.06 M, the pitting potential E_{pit} of SLMed-AlSi10Mg decreases with chloride concentration. However, in present 0.6 M NaCl solution the difference between E_{corr} and E_{pit} vanishes, ie., $E_{\mathrm{pit}} = E_{\mathrm{corr}}$. Fig. 6 shows the corrosion morphology before the reversed scan under optical microscopy. Pitting is obvious for SLMed-AlSi10Mg while it's difficult to distinguish the pitting from the severe uniform corrosion for A360 alloy.

The scan direction is reversed when i_a exceeded 1 mA/cm^2. It's evident that the reverse curve exhibits a larger i_a than that before the inflection, due to pit propagation and the formation of new pits. E_{ptp} has been found a stable electrochemical parameter independent of the reversal point in related works [33–35]. Yasuda *et al.* [33] suggested that E_{ptp} corresponds to the full repassivation of small pits and the initial stages of repassivation of deeper pits. E_{prot} represents complete repassivation of all pits, and it was found in [35] that E_{prot} decreased with an

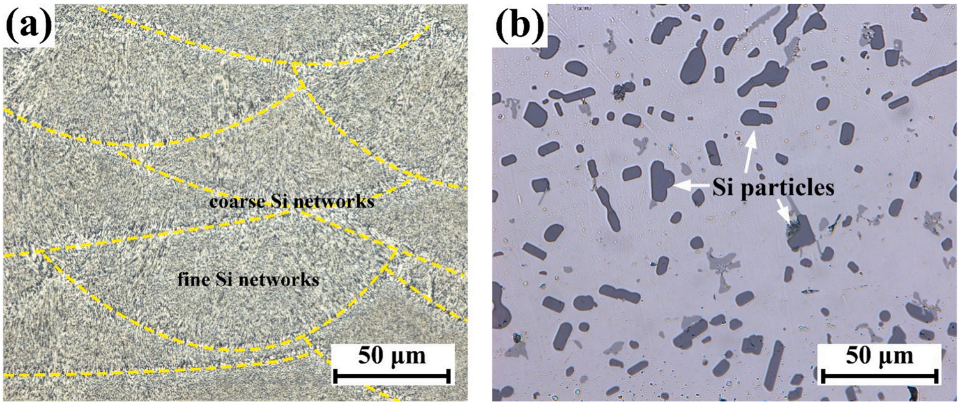

Fig. 3. Microstructure of (a) SLMed-AlSi10Mg and (b) A360 alloys.

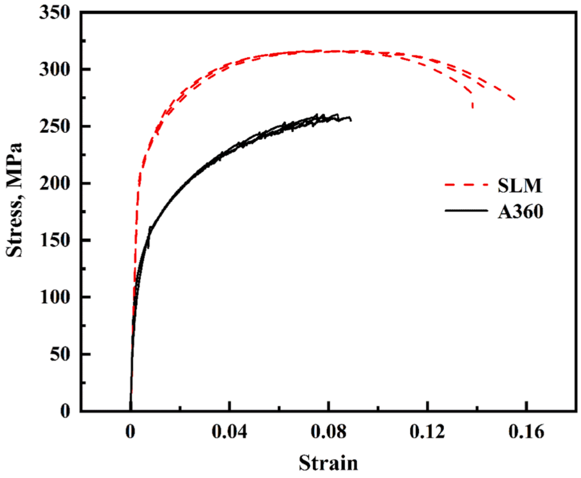

Fig. 4. Tensile stress-strain curves of the SLMed-AlSi10Mg and A360 alloys.

Table 3
Tensile properties and Vicker hardness of the SLMed-AlSi10Mg and A360 alloys.

Material	UTS, MPa	YS, MPa	EL, %	Vicker hardness, $H_{v0.2}$
SLMed-AlSi10Mg	316	217	15.0	103.0
A360 alloy	255	115	8.5	103.5

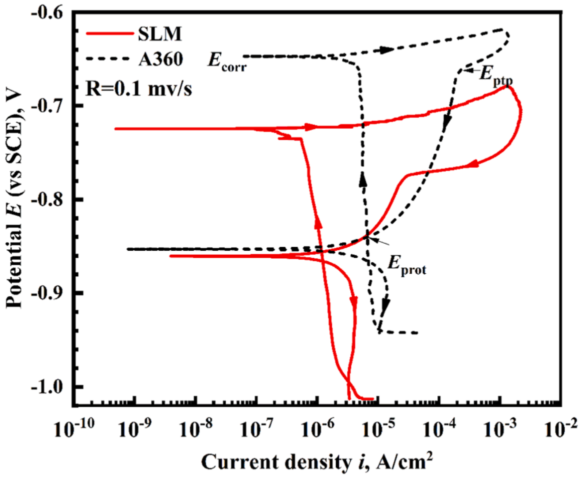

Fig. 5. CPDP curves of the SLMed-AlSi10Mg and A360 alloys.

Table 4
Parameters for fitting the CPDP curves.

Material	E_{pit} (E_{corr}), mV	E_{ptp}, mV	E_{prot}, mV
SLMed-AlSi10Mg	−724	−775	−856
A360	−647	−664	−840

increase in reversed current due to continued pit propagation. The hysteresis observed between the forward and reverse scans indicates the accumulated damage deriving from pitting attack.

The E_{corr} of SLMed-AlSi10Mg is 77 mV lower than A360, indicating the latter possesses higher resistance to pitting corrosion. The results can be explained by the microstructure feature and corrosion morphology shown in Fig. 7. The small spacing and size of the Al cells and Si network in SLMed-AlSi10Mg may reduce the potential difference, causing pitting at a more negative potential compared to A360. However, the passive film on SLMed-AlSi10Mg is likely to be more compact which corresponds to fewer corrosion sites. In contrast, the large Si particles and other secondary phases in A360 alloy disrupt the continuity of the passive films, creating more corrosion sites.

The larger variance between the E_{pit} and E_{ptp} for SLMed-AlSi10Mg (51 mV for SLMed-AlSi10Mg *vs.* 17 mV for A360) suggests higher resistance to repassivation of small pits. On the other hand, the larger variance between E_{pit} and the E_{prot} for the A360 alloy may indicate greater difficulty in fully repairing the passive films, probably due to more severe corrosion damage. The CDPD curve tests were repeated for at least 3 times. The electrochemical parameters obtained varied with each test but the variation was much smaller than the difference between the two alloys. (eg. $E_{corr}= -729$ mV for SLMed-AlSi10Mg and $E_{corr}= -635$ mV for A360 alloy in a repeated test) And it doesn't affect the analysis above.

3.2.2. *Corrosion morphology*

Fig. 7 shows the representative corrosion morphologies pre-corroded specimens at three different magnifications. For SLMed-AlSi10Mg, some ellipsoidal pits in Fig. 7(a, c, e) can be observed. In contrast, signs of uniform corrosion are minimal since the surface generally remains intact. Fig. 7(e) shows the morphology around a pit, where residual Si networks inside the pit suggest selective corrosion of the Al matrix. Fig. 8 illustrates the profile of a typical pit in SLMed-AlSi10Mg observed by a laser confocal microscope which reveals a 50 µm wide and 4 µm deep pit.

In contrast, the A360 alloy exhibits a high density of pits and corrosion products in Fig. 7(b, d). The EDS elemental mapping of Si in the top-right corner of Fig. 7(f) along with the corrosion morphology indicate corrosion is mainly concentrated around the Si particles due to the potential difference between the Al and Si phases. The small and shallow pits in A360 alloy are difficult to identify under laser confocal

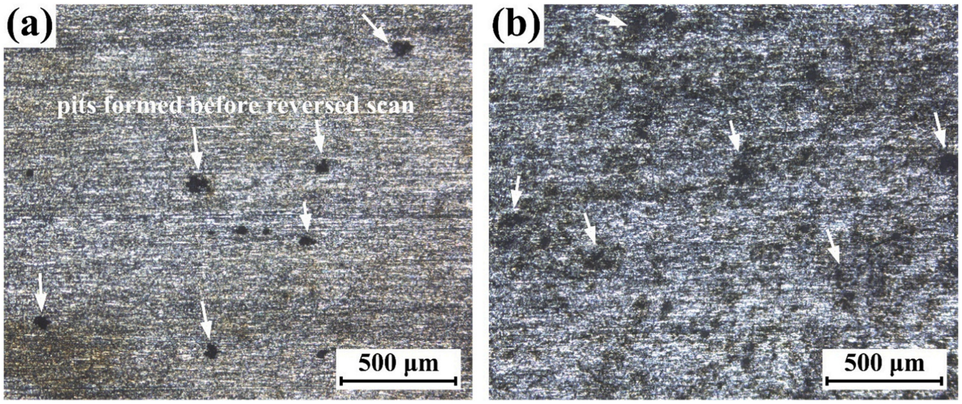

Fig. 6. Pitting morphology before the reversed scan under optical microscopy. (a) SLMed-AlSi10Mg, (b) A360.

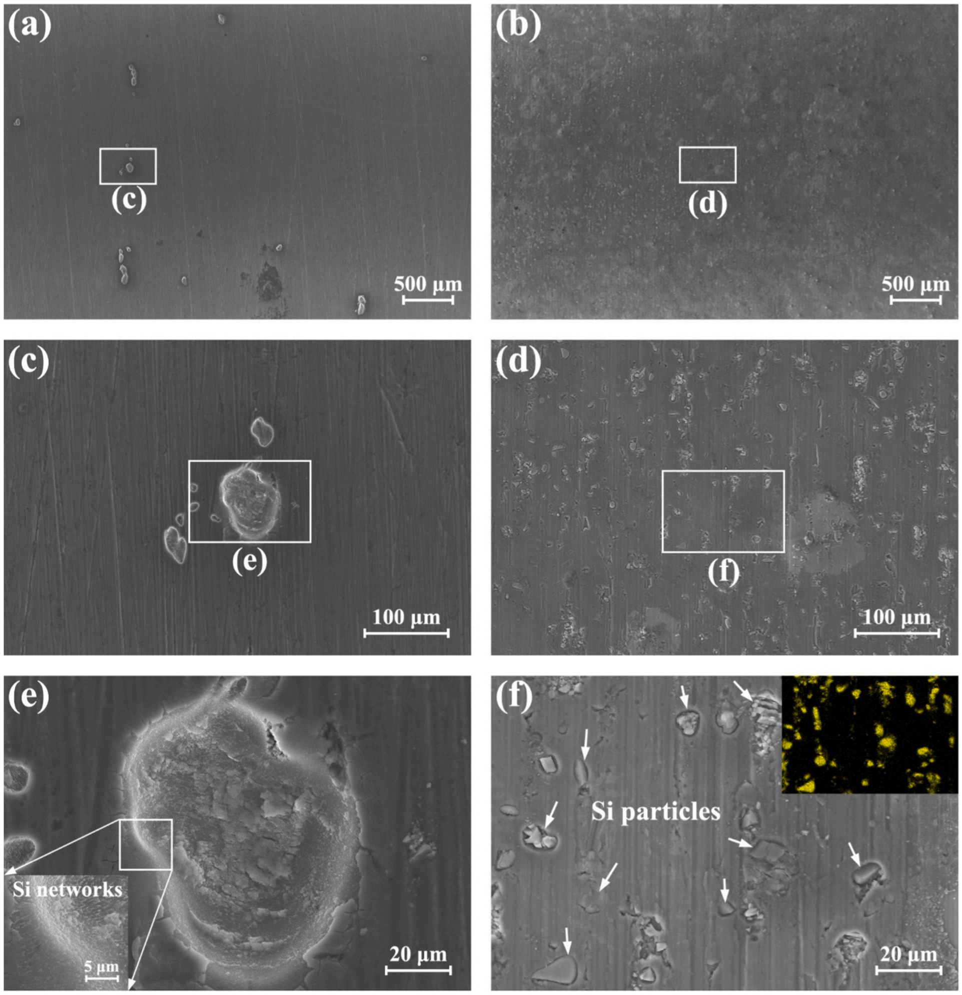

Fig. 7. Morphology after 72 h corrosion tests. (a), (c), (e) PF-SLM; (b), (d), (f) PF-A360.

microscope. Meanwhile, the severe corrosion damage may indicate higher corrosion rate and low resistance to uniform corrosion.

The different corrosion behavior of the two alloys can be attributed to their distinct microstructure. The uniform and fine structure of SLMed-AlSi10Mg may promote the formation of continuous and uniform passive films. Since the local weak points are few the pit can grow rapidly once initiated. In contrast, the large Si particles and other secondary phases containing Fe in the A360 alloy could easily disrupt the continuity of the passive film, leading to a higher probability of small and shallow pits. This behavior aligns with the understanding that pits tend to be shallower when their density is high [15].

The resistance to pitting corrosion is generally higher when the density of initiated pits is high. For example, the addition of Fe can increase the number of cathodic sites (e.g. Al_3Fe intermetallics), thereby increasing the resistance to pitting corrosion [15]. However, pitting sensitivity in aluminum alloys is typically assessed by pit penetration rather than pitting probability [15]. Therefore, SLMed-AlSi10Mg exhibits higher pitting sensitivity than the A360 alloy.

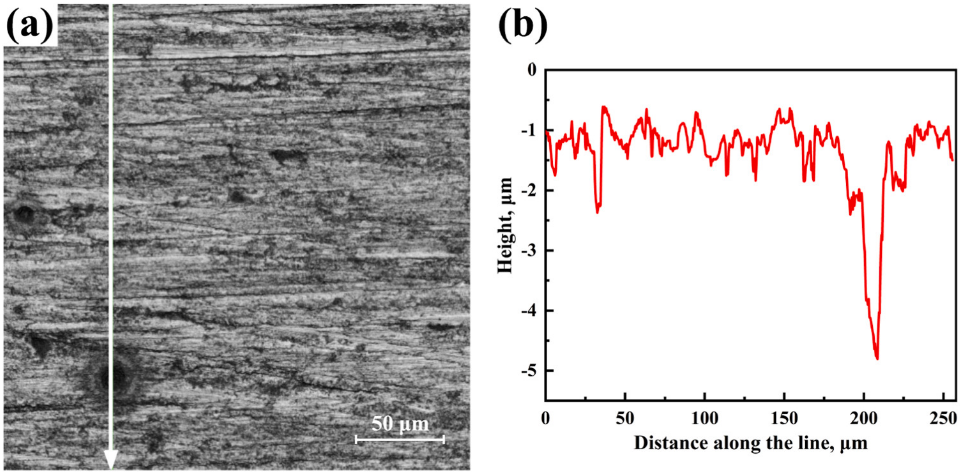

Fig. 8. Surface profile of a PF-SLM specimen. (a) corrosion morphology, (b) profile along the white line in (a).

3.3. *S-N* data

The fatigue results of the two alloys are summarized in Fig. 9. There are 2 or 3 specimens tested at most stress levels to show the dispersion of *S-N* data for both alloys. Fig. 9(a-b) compare the *S-N* data of SLMed-AlSi10Mg and A360 in both air and solution environments. It is evident that the fatigue and corrosion fatigue performances of SLMed-AlSi10Mg are both slightly lower than A360, despite superior strength and ductility of SLMed-AlSi10Mg. Under AF condition, the conditional fatigue limits at 10^7 cycles for the two alloys are very close, i.e., 154 MPa for SLMed-AlSi10Mg and 150 MPa for A360. It's noted that the fatigue limits were calculated using the modified staircase method according to ISO 12017 [36]. Most related works [8–10,13,14] showed that the presence of defects formed during the SLM process were responsible for this worse fatigue performance. Additionally, there is significant dispersion in the *S-N* data for SLMed-AlSi10Mg, which can be attributed to variations in defect sizes, shapes and locations.

Under corrosion fatigue conditions, there appears to be no definitive

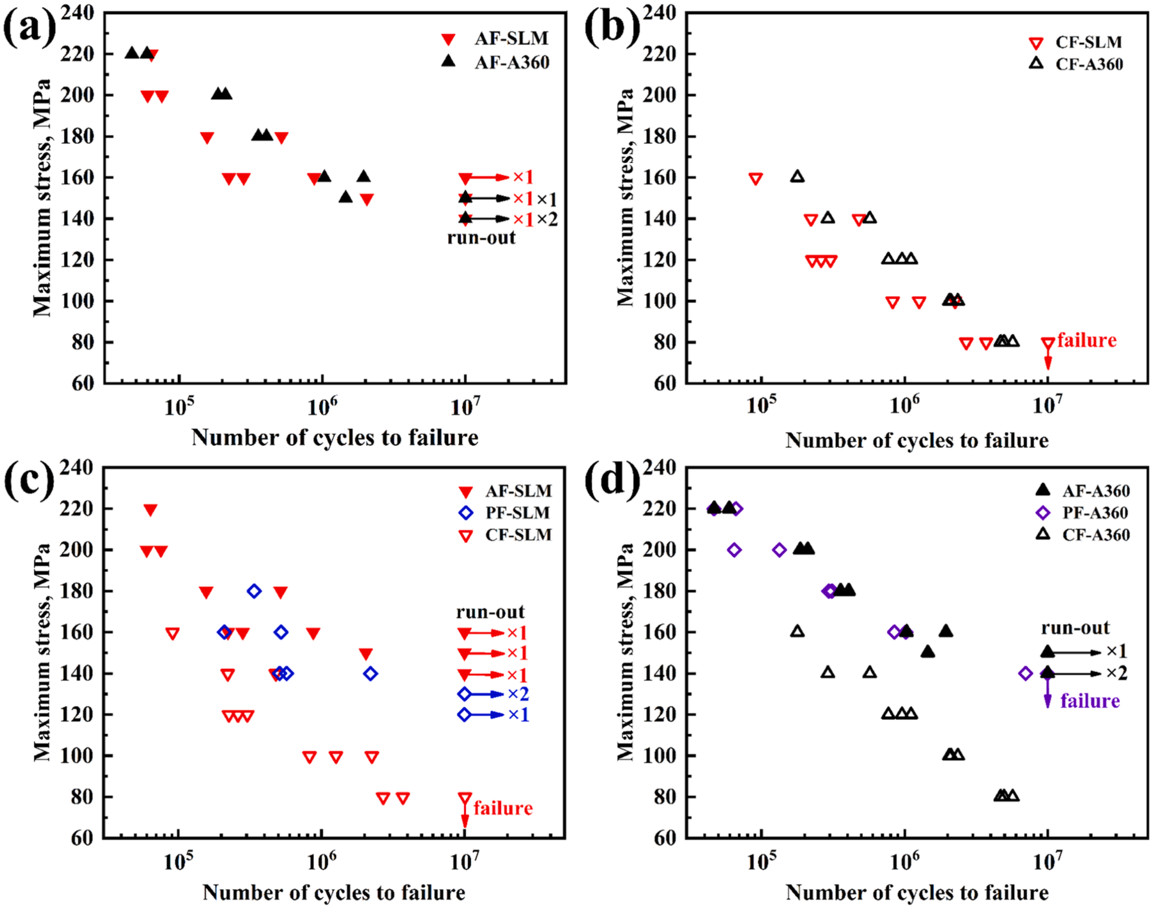

Fig. 9. Comparison of *S-N* curve of SLMed-AlSi10Mg and A360 alloys. (a) AF condition of both alloys, (b) CF condition of both alloys, (c) AF, PF and CF conditions of SLMed-AlSi10Mg, (d) AF, PF and CF conditions of A360 alloy.

fatigue limit at 10^7 cycles for either alloy, as the specimens continue to fail with decreasing stress. The dispersion in the *S-N* data for SLMed-AlSi10Mg remains higher than the A360 alloy. It should be noted that at $S_{\max} = 80$ MPa, two data points of A360 are so close that they are difficult to distinguish ($N_1 = 4693,068$, $N_2 = 4957,111$). Unlike the AF condition exhibiting a fatigue limit, the CF condition allows for millions of cycles at low stress levels which implies the disappearance of the fatigue limit due to corrosion.

Fig. 9(c-d) compare the *S-N* data of the two alloys under AF, PF (prior corrosion fatigue) and CF conditions. Prior corrosion has a limited impact on the *S-N* data of SLMed-AlSi10Mg because LOF defects and pits shows similar sizes evidenced by the following fractography analysis. It can be concluded that prior corrosion may reduce the upper limit of the *S-N* curve, as pits can serve as crack initiation sites when large LOF defects are not present on the surface. However, CF performance shows a significant decrease relative to AF performance, highlighting the importance of the combined effects of cyclic stress and the solution environment.

Similar results are observed for the A360 alloy. There is only a negligible decrease in fatigue life under PF conditions, as the shallow pits cause only weak stress concentrations. It's interesting to note that the PF condition also exhibits no fatigue limit at 10^7 cycles (e.g., one specimen failed at 140 MPa after 9950,468 cycles). Moreover, a significant decrease in the *S-N* data under CF conditions is also apparent which also emphasizes the importance of coupled effect of corrosion and fatigue.

3.4. Fractography

In determining the possible failure mechanisms under different environments the fatigue initiation regions were observed for all specimens. Figs. 10–13 show typical fracture morphologies of SLMed-AlSi10Mg and A360 alloys under air fatigue and corrosion fatigue conditions, respectively. Three distinct regions can be identified for each specimen: crack initiation, crack propagation and final fracture region. The boundary between the crack propagation region and final fracture region were circled by the black dotted lines. Fig. 10(a) presents a global view of the fractured surface of the AF-SLM specimen. The fatigue crack clearly originates from an LOF defect in Fig. 10(b). In fact, all fatigue cracks in AF-SLM specimens initiated from LOF defects as shown in Fig. A1. The size of the fatigue initiation defect is characterized using the equivalent diameter, which is defined as the diameter of a circle with the same area as the LOF defect. The variation in defect sizes is responsible for the scatter in fatigue lives.

Alternating fine and coarse facets are observed in the crack propagation regions in Fig. 10(c-e), indicating that the crack propagates through the center and boundaries of the molten pools sequentially. In the final fracture region (Fig. 10(f)) it shows fine dimples with similar size to Si networks.

For the CF condition, the failure mechanisms for both alloys depend on the applied stress levels. For SLMed-AlSi10Mg, when the maximum stress $S_{\max}$ is above 120 MPa, LOF defects are found as primary crack initiation sites. However, when $S_{\max}$ falls below 100 MPa corrosion pits

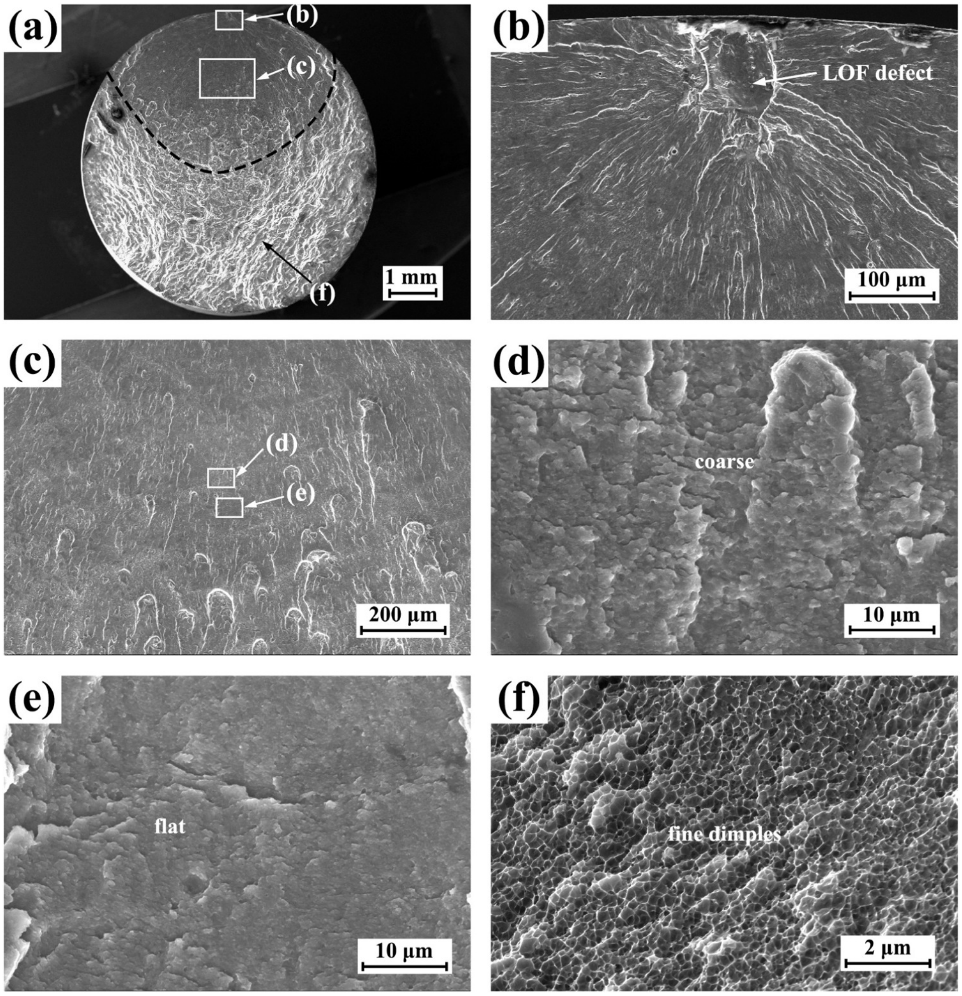

Fig. 10. Fracture surfaces of the AF-SLM specimen, $S_{\max}$= 200 MPa, $N = 75,633$. (a) global view, (b) fatigue initiation, (c) crack propagation, (d) coarse facet, (e) fine facet, (f) final fracture.

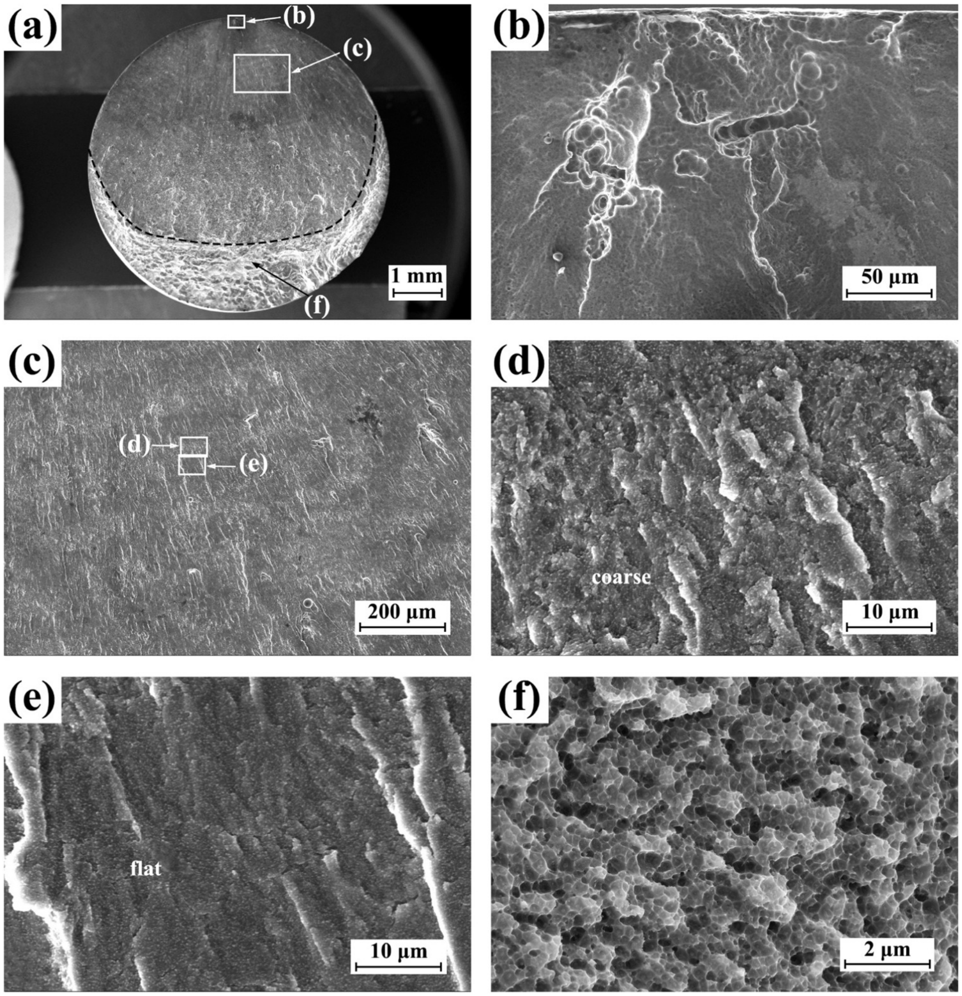

Fig. 11. Fracture surfaces of the CF-SLM specimen, $S_{\max}$= 80 MPa, N = 2701,133. (a) global view, (b) fatigue initiation, (c) crack propagation, (d) coarse facet, (e) fine facet, (f) final fracture.

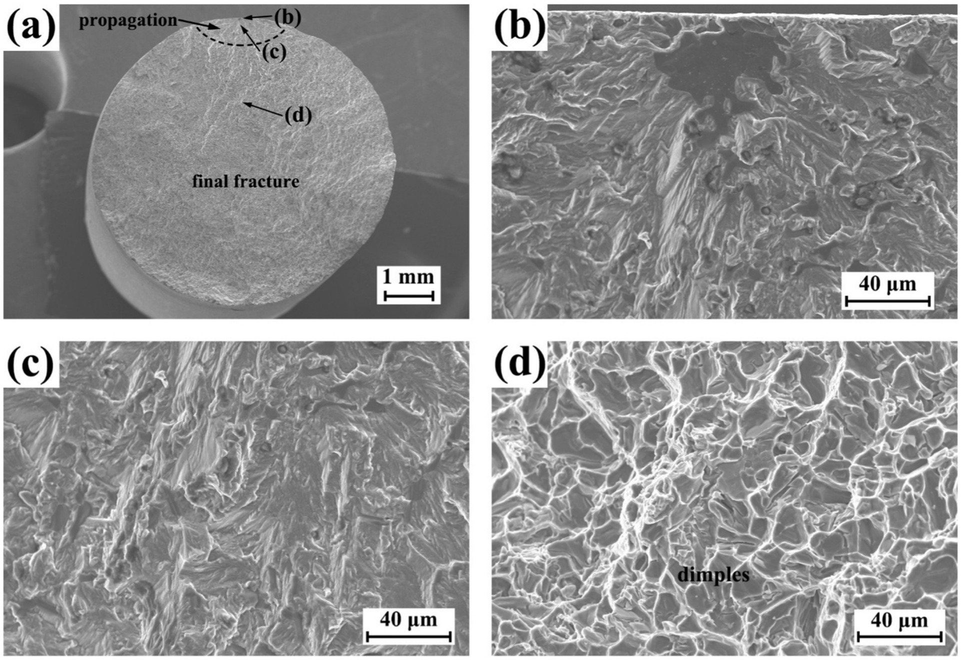

Fig. 12. Fracture surfaces of the AF-A360 specimen, $S_{\max}$= 200 MPa, N = 210,552. (a) global view, (b) fatigue initiation, (c) crack propagation, (d) final fracture.

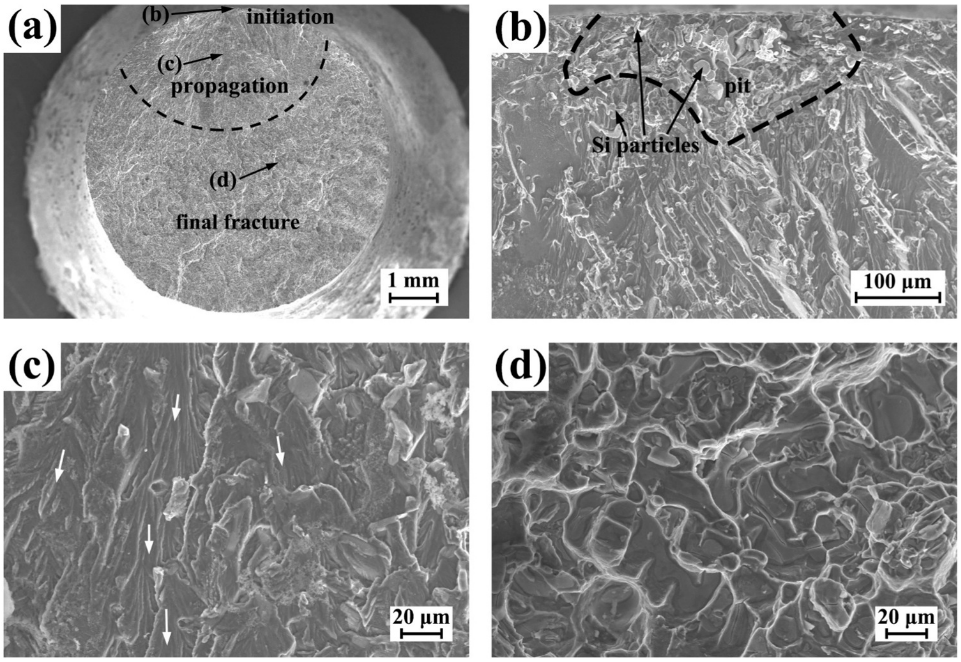

Fig. 13. Fracture surfaces of the CF-A360 specimen, $S_{\max}$= 100 MPa, N = 2057,134. (a) global view, (b) fatigue initiation, (c) crack propagation, (d) final fracture.

become the dominant initiators. All the crack initiation regions of CF-SLM specimens are shown in Fig. A2. Similar to the AF condition larger LOF defects are associated with shorter fatigue lives at the same stress level. And the variation in defect sizes contributes to the dispersion in the *S-N* data.

Fig. 11 shows the fractured surfaces of the CF-SLM specimen subjected to $S_{\max}$ of 100 MPa. The crack initiation clearly occurs at a pit in Fig. 11(b). However, it's important to note that the micromorphological features of pits vary between specimens, which could be divided into 3 types: 1) continuous pit penetration in Fig. A2(h-i), 2) localized corrosion with numerous separate semi-ellipsoidal pits on the lateral face in Fig. A2(j-k) and 3) two adjacent semi-ellipsoidal pits in Fig. A2(l) resembling surface pitting. The severe corrosion during the initiation stage suggests an incubation period where the crack propagation rate is initially slower than the pitting rate, which is also supposed by previous works [37–39].

In the crack propagation region alternately coarse and flat facets are also observed as shown by Fig. 11(c-e). It is unclear whether the residual Si particles were formed during crack propagation because the fresh surface continued to corrode afterward. In the final fracture region in Fig. 11(f), fine dimples with similar size to the Si networks could also be observed which shows no clear difference from the AF specimens.

Fig. 12(a) presents a global view of the fracture surface of the AF-A360 specimen. A cleavage plane is found in the initiation region of Fig. 12(b). This suggests that cyclic dislocation slip along specific crystal plane and damage accumulates within a single grain. It is important to note that the cycles for the formation of cleavage planes may account for a substantial proportion of fatigue life.

The crack propagation region of A360 specimen is relatively small when compared to SLMed-AlSi10Mg due to the lower toughness of the former. The fluctuating features observed in Fig. 12(b-c) may indicate greater resistance to crack propagation. Ductile dimples with size of 20 µm are visible in the final fracture region as shown by Fig. 12(d).

Fig. A3 shows the fatigue initiation regions of all CF-A360 specimens. When $S_{\max}$ is above 120 MPa, cleavage planes can traverse several grains as shown by Fig. A3(a-d, f) except one specimen (Fig. A3(e)) failing due to a pit. This observation supports the anodic dissolution-assisted slip mechanism [16–18]. When $S_{\max}$ is below 100 MPa corrosion becomes the primary factor in initiating the fatigue crack. The fatigue lives are nearly proportional to the pit depth without considering the stress level as shown by Fig. A3(g-l).

Fig. 13(a) provides a typical global view of a CF-A360 specimen failed under low stress conditions. In contrast to the tiny surface pitting, the initiation site shows similar morphologies for different specimens with numerous Si particles distributed as shown by Fig. 13(b). In the propagation region (Fig. 13(c)) it shows a river pattern and Si particles which may indicate the effect of anodic dissolution. No significant difference is detected in the final fracture region between AF and CF conditions as shown by Fig. 13(d).

For PF-SLM specimens, pits can also act as stress concentrators and lead to crack initiation as shown in Fig. 14. The two neighboring pits are nearly 100 µm in width and 25 µm in depth which are comparable to LOF defects. Fig. 14(b) shows residual Si networks inside the pits which is consistent with the selective corrosion of Al matrix mechanism. However, for other specimens cracks all initiated from LOF defects. This indicates that while both pits and LOF defects can compete in initiating fatigue cracks, LOF defects may be more detrimental due to their greater depth. For PF-A360 specimens, no different failure features were observed compared to the AF condition as shown by Fig. 14(c-d).

4. Discussion

4.1. *Analysis of S-N data dispersion*

The *S-N* data for the SLMed-AlSi10Mg exhibit greater dispersion compared to the A360 alloy regardless of the environment. For AF-SLM specimens, this dispersion is primarily due to factors such as the location, shape, and size of defects, among which the defect size is consider to be the most significant factor in [13,14]. Tiryakioglu *et al.* [40,41] proposed Eq. (1) to describe the effects of defect size on the *S-N* data dispersion. The equation has been successfully used in the fatigue assessment of A356 aluminum and Al-7Si-0.6Mg-0.11Fe alloys [41]. This equation assumes that the initiator size follows a Gumbel distribution and relates fatigue life to defect size using Paris power law:

$$P_f = 1 - \exp\left[-\exp\left(-\frac{\left(N\cdot S_{\max}^m/B\right)^{2/(2-m)} - \mu_G}{\sigma_G}\right)\right] \tag{1}$$

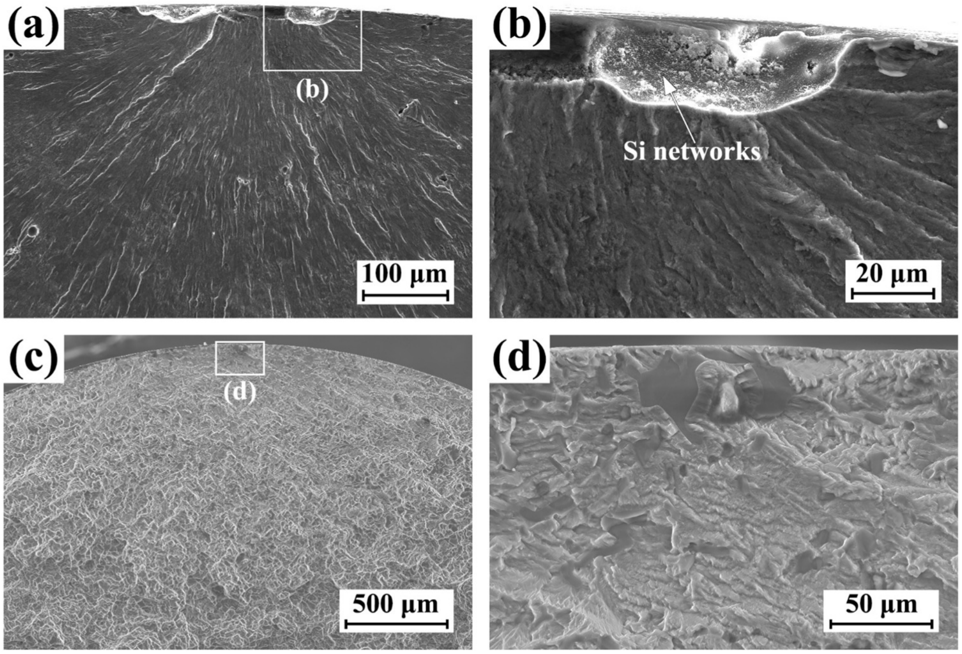

Fig. 14. Fracture surfaces of PF specimens. (a), (b) PF-SLM, $S_{\max}$= 180 MPa, $N = 340{,}055$, initiation from pitting, (c), (d) PF-A360, $S_{\max}$= 180 MPa, $N = 309{,}968$, initiation from cyclic slip.

Here, P_f is the failure probability, m is the Paris exponent, μ_G and σ_G are the location and scale parameters of Gumbel distribution, B is a material constant, N is the fatigue life and $S_{\max}$ is the maximum stress.

The Frechet distribution was also considered for statistical analysis of fatigue initiator size according to [42]. The Frechet distribution is a type II extreme value distribution in which the variable has a lower limit. According to [42] the prediction of *P-S-N* curves using Frechet distribution is given as:

$$P_f = 1 - \exp\left[-\left(\frac{\left(N \cdot S_{\max}^m / B\right)^{2/(2-m)}}{\sigma_F}\right)^{-\alpha_F}\right] \tag{2}$$

Here, P_f is the failure probability, m is the Paris exponent, α_F and σ_F are the shape and scale parameters of Frechet distribution, B is a material constant, N is the fatigue life and $S_{\max}$ is the maximum stress.

Fig. 15 compares the predicted *P-S-N* curves obtained from Eqs. (1) and (2). It is evident that the *S-N* data generally fall within the predictions of both approaches, but the Frechet approach appears to be more conservative. This conservatism reflects a different prediction capability regarding the upper limit of fatigue initiation defect size. With the optimization of SLM process, the size of LOF pores or gas pore may be further controlled and hence improve the fatigue performance and reduce the *S-N* data dispersion in air. The conducted analysis of fatigue dispersion would also be helpful for the quality assessment of materials formed with other processing parameters.

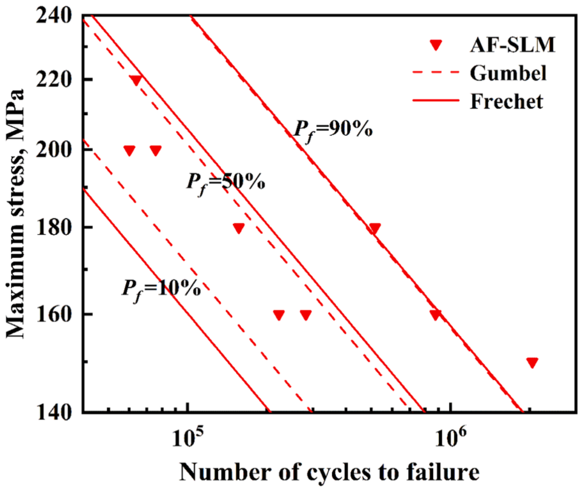

Fig. 15. Prediction of *P-S-N* curves for the AF-SLM specimens.

For CF condition the dispersion may also originate from the fatigue initiation process because of large randomness in corrosion but stable macrocrack growth dominated by the cyclic stress intensity factor ΔK. The growth of pitting is usually considered to follow a power equation ($d \propto t^{1/3}$) by assuming that the quantity of dissolved metal during a time interval is constant [15], which means the penetration rate will gradually be slower with increasing pitting size. For A360 alloy the depth of fatigue initiation pitting is nearly proportional to the fatigue life. e.g., $S_{\max}$= 100 MPa, $N \approx 2 \times 10^6$, $d \approx 100$ µm and Fig. A3(j-l), $S_{\max}$= 80 MPa, $N \approx 5 \times 10^6$, $d \approx 200$ µm as shown by Fig. A3(g-l). A stable corrosion process may be the reason why the *S-N* data is less dispersed.

For SLMed-AlSi10Mg the dispersion at high stress levels of CF condition also mainly depends on the size of LOF defects. However, fatigue initiation pitting at low stress levels showed similar sizes but different morphologies and features. Although different failure mechanisms are involved in CF conditions, the dispersion of *S-N* data can be assessed using traditional methods [43,44] that do not account for the influence of defect or pitting sizes. A median *S-N* curve was first fitted by Basquin equation (Eq. (3)), and then *S-N* data were transformed into fatigue lives at the same stress level by the exponent b. The fatigue lives were ranked and fitted using the two-parameter Weibull distribution (Eq. (4)). The *P-S-N* curves at certain failure probabilities (P_f=10 %, 50 % and 90 %) could be obtained considering the corresponding fatigue lives and Eq. (3). For comparison, the *S-N* data of the CF-A360 specimens were also analyzed using the same approach as shown by Fig. 16.

$$C = S_{\max} \cdot N^b \tag{3}$$

$$P_f = 1 - \exp\left[-\left(\frac{N}{N_0}\right)^{b_n}\right] \tag{4}$$

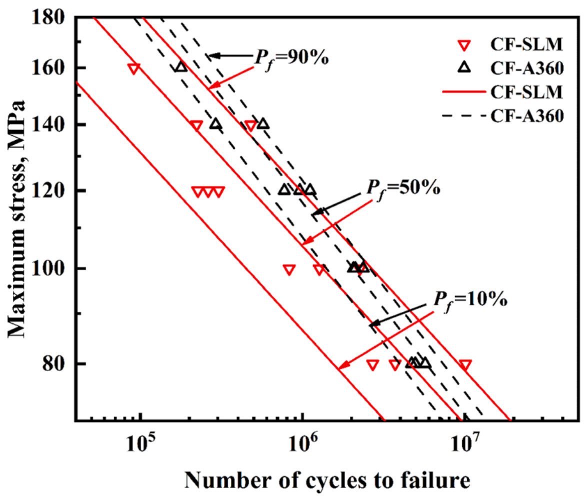

Fig. 16. Predictions of *P-S-N* curves for the CF-SLM and CF-A360 specimens.

Here, b and C are material constants that varied with failure probability, $S_{\max}$ and N are the maximum stress and fatigue life; P_f is the failure probability, N_0 is the scale parameter, and b_n is the shape parameter. It's clear that almost all the *S-N* data fall within the predicted range because the fitting is self-consistent. Here, b_n reflects the horizontal width of the scatter band. The smaller b_n, the larger the fatigue life dispersion ($b_n \approx 1.7$ for CF-SLM and $b_n \approx 5$ for CF-A360 means the horizontal width of the scatter band of the former is about 3 times of the latter in log-log plot). Different failure mechanisms in SLMed-AlSi10Mg makes it difficult to accurately predict *S-N* data particularly under CF conditions. Therefore, it should be cautious to consider environmental effects to ensure the safety of additive manufacturing components during service.

4.2. Corrosion effect on the fatigue initiation mechanisms

The fatigue failure mechanisms of SLMed-AlSi10Mg and A360 alloy under AF, PF and CF conditions were schematically shown in Fig. 17. In air LOF defect and cyclic slip serve as the fatigue initiators for SLMed-AlSi10Mg and A360 alloy, respectively. Prior corrosion just has negligible influence on the fatigue performance and failure mechanisms of both alloys. For PF-SLM specimens pits may play a competition role with LOF defects in fatigue initiation only if the pits grow large enough. While for PF-A360 specimens there are only tiny pits which could not lead to enough stress concentration to initiate a crack. But for other aluminum alloys [23,25] with no reported processing defects, it was found prior corrosion could clearly reduce the fatigue performance. Guérin *et al.* [23] reported that the higher sensitivity to prior corrosion of T34 tempered 2050 alloy was due to intergranular corrosion formed in the first several minutes. Rochet *et al.* [25] found that prior corrosion for 72 h at E_{corr} could lead to a more than 90 % decrease in fatigue lives of an equal-channel angular pressed Al-Si-Mg alloy due to the corrosion defects formed by dissolution around the Fe-rich intermetallic. The lower fatigue sensitivity to prior corrosion of SLMed-AlSi10Mg could attribute to the limited pitting penetration than LOF defects. And tiny shallow pits with little stress concentration results in the low sensitivity to prior corrosion for A360 alloy.

However, the CF failure mechanisms of SLMed-AlSi10Mg and A360 alloys exhibit different features with AF and CF conditions. The failure mechanisms of both alloys vary with stress levels, which are consistent with the results for other aluminum alloys in several previous studies [16–18,21]. Lin. et al. proposed a slip-induced anodic dissolution mechanism for CF initiation of 7050 aluminum at high stress level as it's difficult for the pit to grow large enough to initiate the fatigue crack in a short fatigue life. And it was found that crack initiation was the dominant process in the CF failure by comparing the *S-N* data and crack propagation rates of T6 and T73 tempers. Gong *et al.* reported CF failure

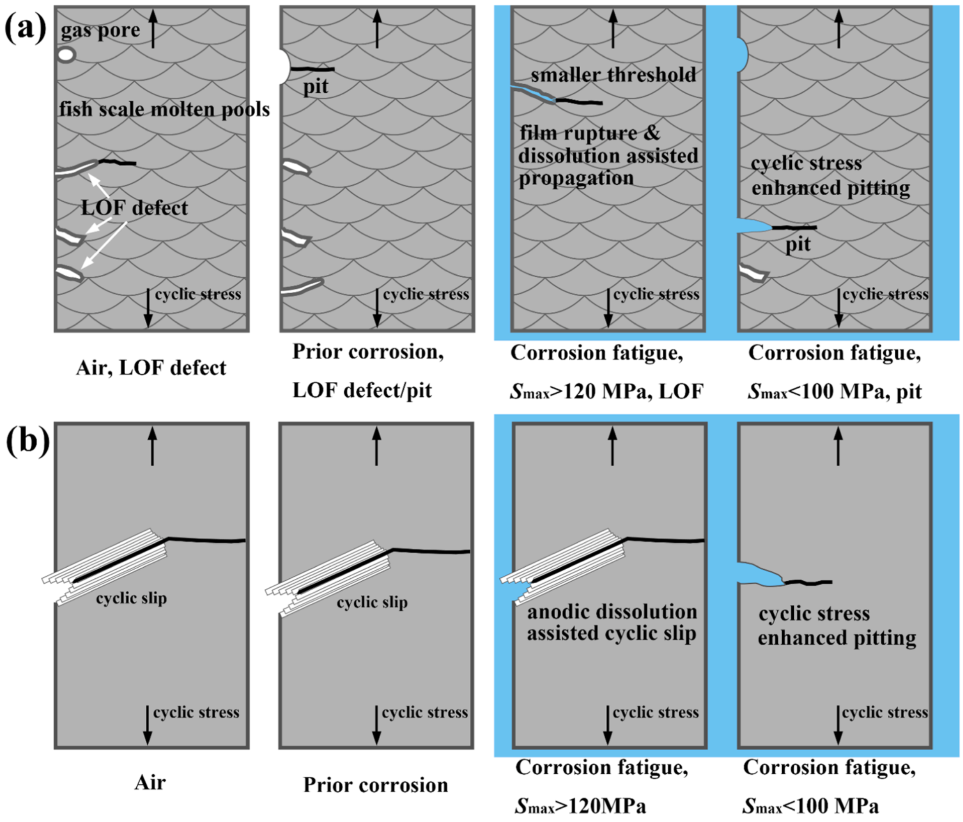

Fig. 17. Schematic diagram of effect of corrosion on the fatigue initiation mechanisms. (a) SLMed-AlSi10Mg, (b) A360 alloy.

of 7075 aluminum alloy was due to dislocation accumulation on the grain boundary at high stress level while pitting-induced crack initiation at low stress level. Sharma. et al. found secondary inclusions and tiny pits acted as fatigue initiator at high stress level while pitting tunnels at low stress level for ultrafine grained Al-7.5Mg alloy. It could be summarized that the CF failure at low stress level is usually due to pitting while it varies with different materials at high stress level.

For both alloys in our study, the CF lives reduced dramatically at high stress level close to the fatigue limit in air. Pitting is not identified as the primary fatigue initiator at these conditions. Instead, the failure mechanism is similar to AF conditions. The fatigue limit of a material containing defects can be described as the stress corresponding to the critical condition for non-propagating cracks [45,46]. This indicates that the threshold of microcrack $\Delta K_{\mathrm{th,sc}}$ significantly decreases in a corrosive environment. For SLMed-AlSi10Mg, considering the combined effects of corrosion and cyclic stress on LOF defects, one possible mechanism is film rupture and anodic dissolution-assisted crack initiation proposed in [16–18]. The effect of cyclic stress is to break down the oxide films in the LOF defect root. Anodic dissolution would also promote the microcrack propagation. As the crack grows, the influence of corrosion may decrease because it's harder for ions to transfer at the crack tip, and mechanical factors become more important. The anodic dissolution assisted slip mechanism may be relevant for the A360 alloy, as evidenced by the deeper penetration of cleavage planes and the residual Si particles in CF specimens compared to AF conditions [16–18].

When pitting dominates the CF failure mechanism, both alloys exhibit similar CF sensitivity despite of different pitting sensitivities. The transition from LOF defects to pitting as the primary fatigue initiator at lower stress levels in SLMed-AlSi10Mg may be attributed to variation of local electrochemical conditions [18]. Galy *et al.* [7] suggested that oxides formed on the surface of the melt pool contribute to defect formation. Cao *et al.* [47] and Olakanmi *et al.* [48] also reported the existence of oxides near the LOF defects. The lateral surface of LOF defects may act as a cathodic site due to the presence of oxides, creating a more positive potential compared to the Al matrix. At low stress level, the oxide film around the LOF defect root may not rupture which would result in the fact that electrochemical process is limited due to more positive potential of oxides at LOF defect root. However, pitting can occur rapidly at local weak points on the surface [20,23]. The relatively open corrosion cavity and continuous anodic dissolution can be further accelerated by cyclic stress. Above process inhibits the passivation of pits and facilitates their growth to a critical size, thus eliminating the fatigue limit. Wang *et al.* [19] reported that deeper corrosion penetration resulted in shorter CF lives for partially recrystallized Al-Mg-Si

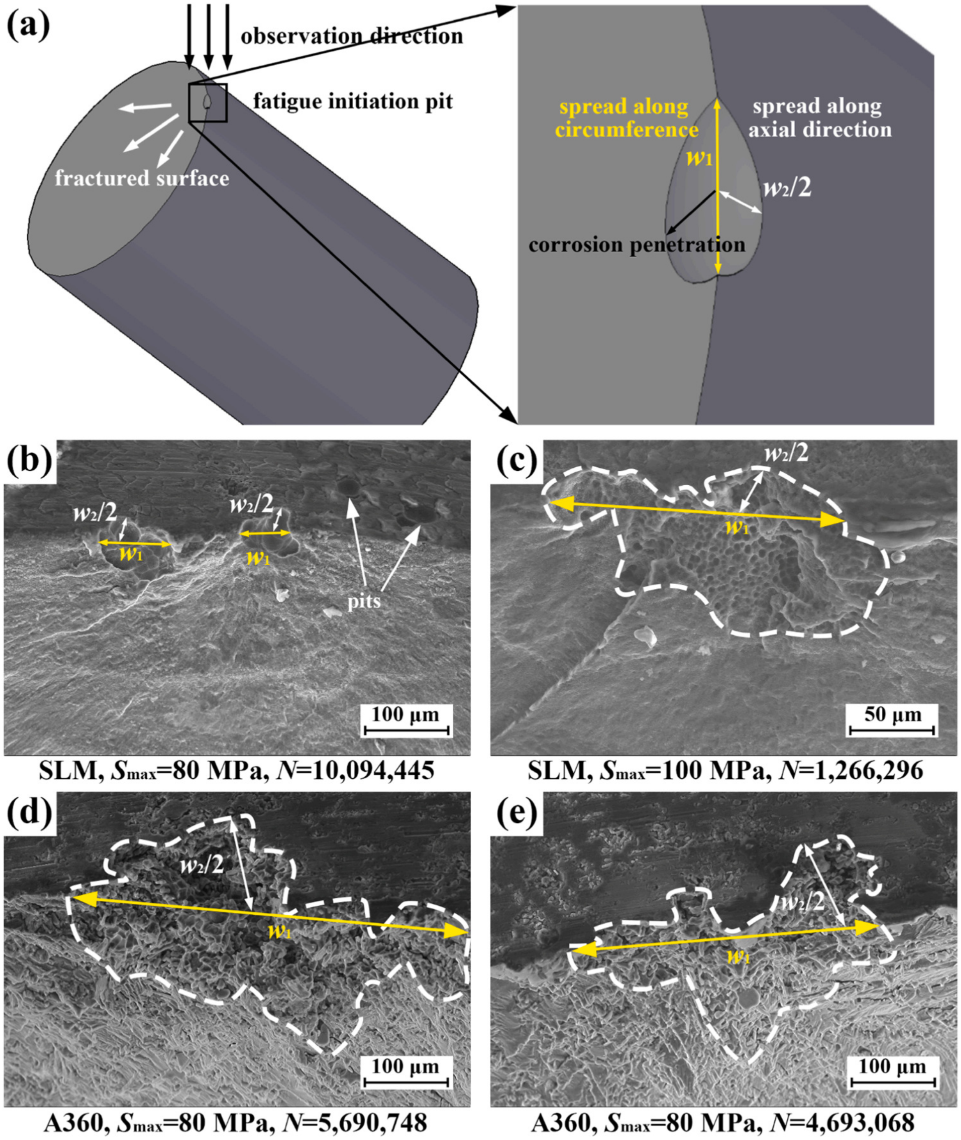
SLM, $S_{\max}$=80 MPa, N=10,094,445

SLM, $S_{\max}$=100 MPa, N=1,266,296

A360, $S_{\max}$=80 MPa, N=5,690,748

A360, $S_{\max}$=80 MPa, N=4,693,068

Fig. 18. Morphology of fatigue initiation pits. (a) schematics, (b), (c) CF-SLM, (d), (e) CF-A360.

alloy. In our study, the fatigue initiation pits of both alloys had similar penetration depths of about 100–200 μm, which were significantly larger than typical surface pits. This suggests the cyclic stress accelerated pitting corrosion mechanism. The fatigue initiation pits of CF-SLM and CF-A360 specimens were examined by SEM in Fig. 18(a). Here, w_1 and w_2 represent the widths of pitting along the circumference and axial direction, respectively. For both alloys w_1 tends to be larger than w_2 indicating that cyclic stress mainly accelerates corrosion perpendicular to the axial direction. Here it is noted that the case in Fig. 18(b) is not applied, which shows initiation from two adjacent semi-elliptical pits. In Rochet *et al.*'s study [25] it was found that the synergy effect of corrosion and fatigue didn't influence the surface pit size but the number density when compared to prior corrosion in a same time interval. But pits were not observed as the CF initiators which may be due to the applied high stress level. This implies that corrosion current may be considered for CF performance as it may have a positive relation with pitting density. If the size of pitting follows a same distribution higher pitting density also represents a higher probability in formation of large pits. The lower corrosion rate of SLMed-AlSi10Mg may offset its higher pitting sensitivity and make it exhibit a similar CF sensitivity with A360 alloy.

5. Conclusions

The conclusions of the study on the fatigue performance of SLMed-AlSi10Mg and A360 alloys under various environmental conditions are summarized as follows:

1. Fatigue Properties: SLMed-AlSi10Mg (SR state) and A360 alloy (T6) exhibit comparable fatigue performance in both air and 0.6 M NaCl solution environments, despite SLMed-AlSi10Mg demonstrating 1.24 times strength and 1.76 times ductility than A360 alloy. Synergistic effects of corrosion and fatigue lead to a clear decrease of in *S-N* data for both alloys. The conditional fatigue limit at 10^7 cycles both reduced more than 50 % in solution environment. While prior corrosion has a negligible influence, highlighting the significant mutual effects of corrosive media and cyclic stress.
2. Fatigue initiation: In air, SLMed-AlSi10Mg shows fatigue initiation primarily from LOF defects with equal diameter ranging from 30 μm to 180 μm, while A360 alloy initiates from surface slip. In 0.6 M NaCl solution, when maximum stress ($S_{\max}$) is above 120 MPa, the initiation mechanisms remain similar to those in air (i.e., LOF defects for SLMed-AlSi10Mg and surface slip for A360). However, when $S_{\max}$ is lower than 100 MPa pitting with penetration higher than 100 μm becomes the dominant initiator for both alloys.
3. Corrosion behavior: SLMed-AlSi10Mg exhibits a 77 mV lower corrosion potential than A360 alloy. The combined effect of pitting sensitivity and corrosion rate results in similar corrosion fatigue (CF) sensitivity for both alloys, despite differences in their inherent corrosion characteristics.
4. Dispersion in *S-N* Data: The *S-N* data of SLMed-AlSi10Mg shows greater dispersion than that of A360 alloy in both air and solution environments. In air, this dispersion primarily results from the size of LOF defects. Under solution environment the dispersion was evaluated using the Weibull shape parameter (b_n), and the results indicated 3 times wider dispersion band of SLMed-AlSi10Mg than A360 alloy.

CRediT authorship contribution statement

Xuechong Ren: Writing – review & editing, Validation, Supervision, Project administration. **Alex A. Volinsky:** Writing – review & editing, Validation, Formal analysis. **Hongqian Chen:** Writing – original draft, Methodology, Formal analysis, Data curation. **Peng Liu:** Writing – review & editing, Validation, Formal analysis.

Declaration of Competing Interest

We declare that we have no known competing financial interests or personal relationships that could have appeared to influence the work reported in this paper.

Acknowledgements

This research was supported by the National Natural Science Foundation of China (11932020).

Appendix A. Fatigue initiation regions of AF-SLM, CF-SLM and CF-A360 specimens

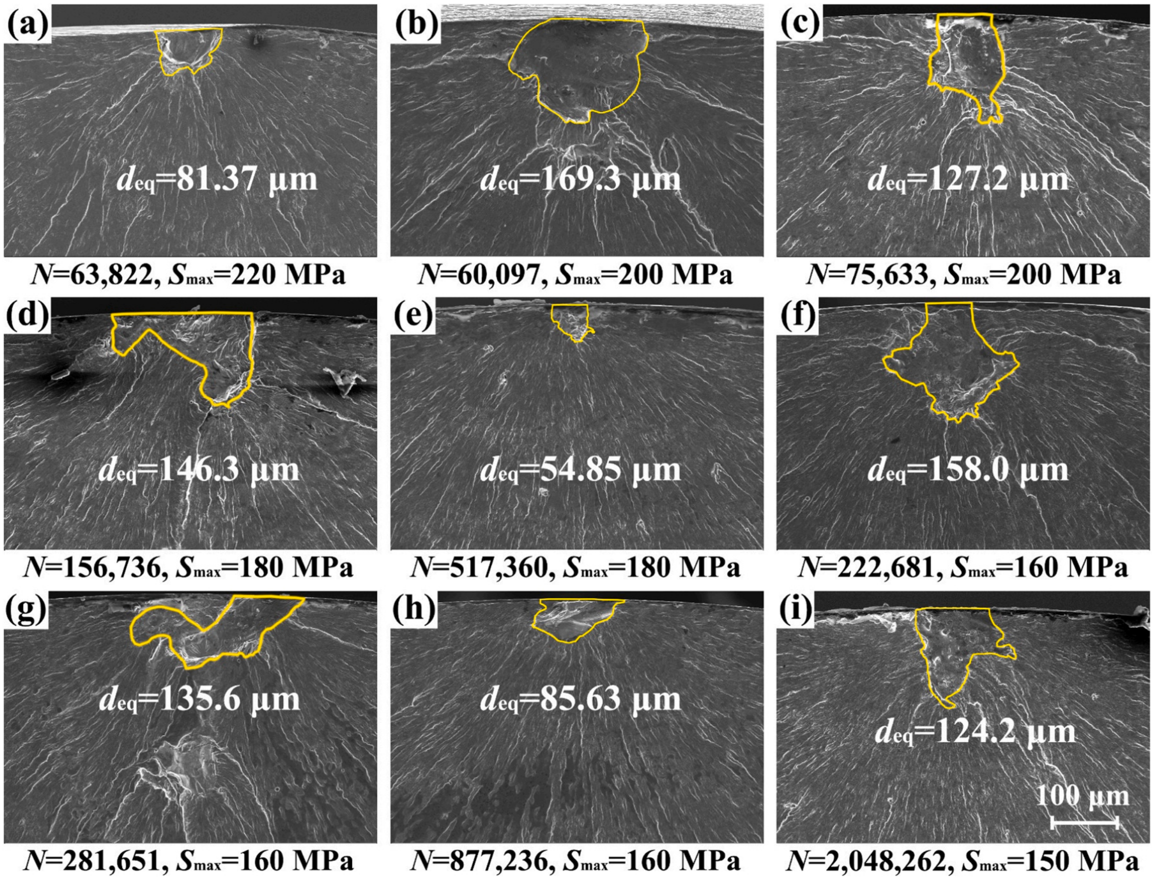

Fig. A1. Fatigue initiation regions of the AF-SLM specimens. (a-i) refer to each of the fractured specimen with the fatigue initiator outlined. [42]

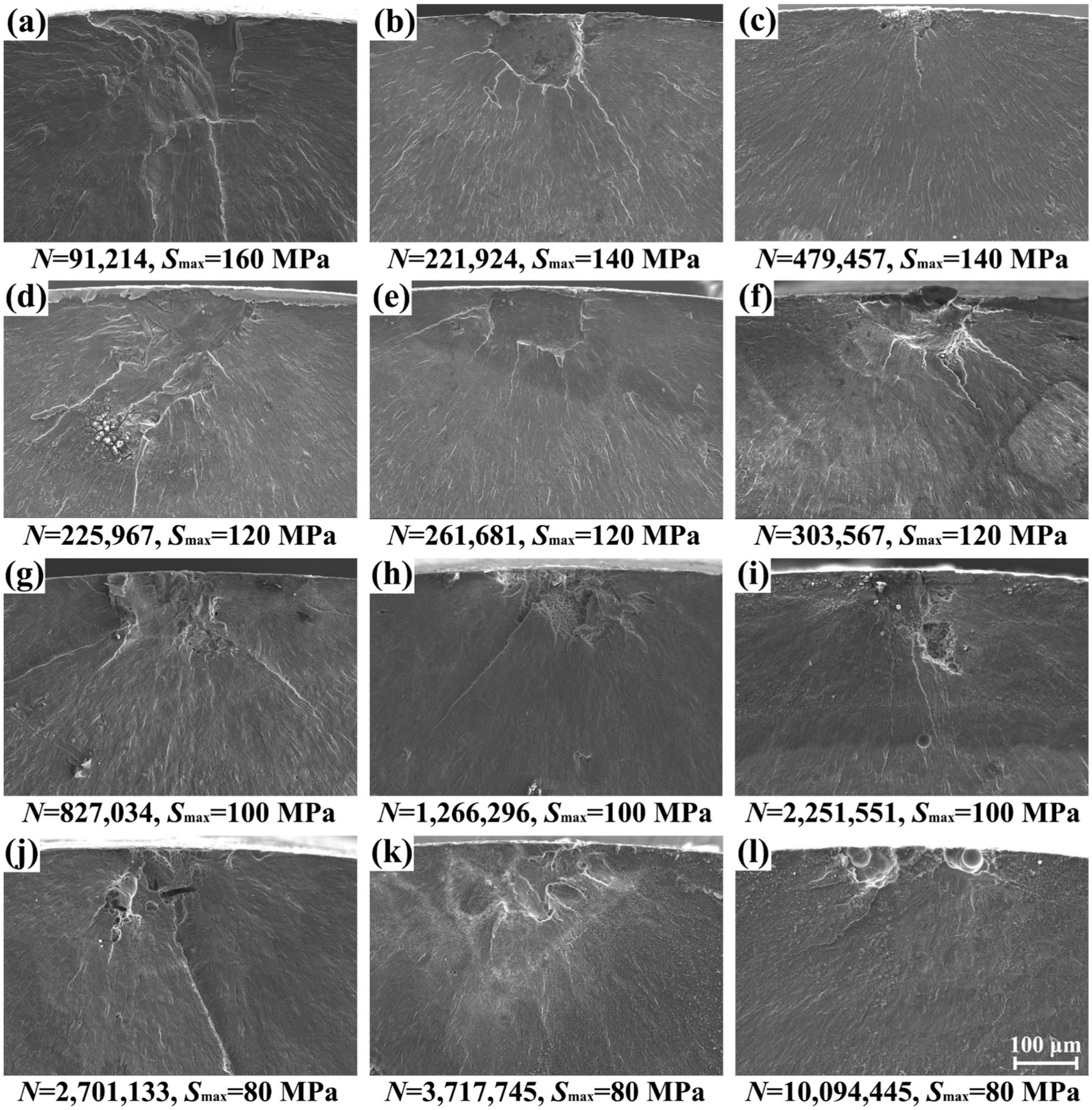

(a) N=91,214, S_{max}=160 MPa
(b) N=221,924, S_{max}=140 MPa
(c) N=479,457, S_{max}=140 MPa
(d) N=225,967, S_{max}=120 MPa
(e) N=261,681, S_{max}=120 MPa
(f) N=303,567, S_{max}=120 MPa
(g) N=827,034, S_{max}=100 MPa
(h) N=1,266,296, S_{max}=100 MPa
(i) N=2,251,551, S_{max}=100 MPa
(j) N=2,701,133, S_{max}=80 MPa
(k) N=3,717,745, S_{max}=80 MPa
(l) N=10,094,445, S_{max}=80 MPa

Fig. A2. Fatigue initiation regions of the CF-SLM specimens. (a-l) refer to each of the fractured specimen

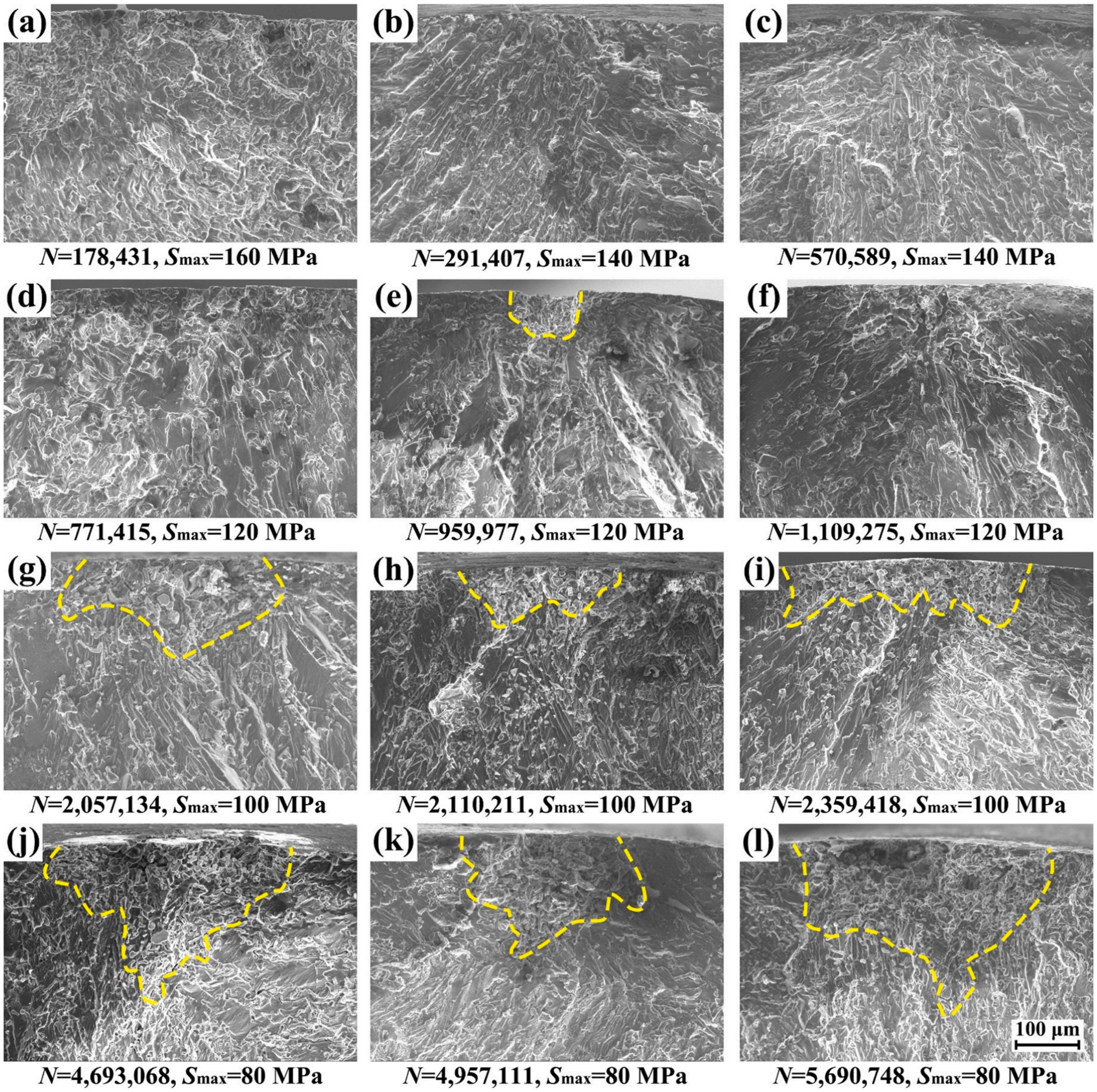

N=178,431, S_{max}=160 MPa

N=291,407, S_{max}=140 MPa

N=570,589, S_{max}=140 MPa

N=771,415, S_{max}=120 MPa

N=959,977, S_{max}=120 MPa

N=1,109,275, S_{max}=120 MPa

N=2,057,134, S_{max}=100 MPa

N=2,110,211, S_{max}=100 MPa

N=2,359,418, S_{max}=100 MPa

N=4,693,068, S_{max}=80 MPa

N=4,957,111, S_{max}=80 MPa

N=5,690,748, S_{max}=80 MPa

Fig. A3. Fatigue initiation regions of the CF-A360 specimens. (a-l) refer to each of the fractured specimen with the fatigue initiator outlined

Data availability

Data will be made available on request.

References

[1] N. Li, S. Huang, G. Zhang, R. Qin, W. Liu, H. Xiong, Progress in additive manufacturing on new materials: a review, J. Mater. Sci. Technol. 35 (2019) 242–269, https://doi.org/10.1016/j.jmst.2018.09.002.

[2] T. DebRoy, H.L. Wei, J.S. Zuback, T. Mukherjee, J.W. Elmer, J.O. Milewski, Additive manufacturing of metallic components-process, structure and properties, Prog. Mater. Sci. 92 (2018) 112–224, https://doi.org/10.1016/j.pmatsci.2017.10.001.

[3] T. Maconachie, M. Leary, B. Lozanovski, X. Zhang, M. Qian, O. Faruque, SLM lattice structures: properties, performance, applications and challenges, Mater. Des. 183 (2019) 108137, https://doi.org/10.1016/j.matdes.2019.108137.

[4] R.N. Lumley, Fundamentals of aluminium metallurgy, Elsevier: Woodhead Publishing, 2018, https://doi.org/10.1016/C2016-0-02117-4.

[5] J. Wu, W.Q. Wang, W. Wang, M.M. Attallah, M.H. Loretto, Microstructure and strength of selectively laser melted AlSi10Mg, Acta Mater. 117 (2016) 311–320, https://doi.org/10.1016/j.actamat.2016.07.012.

[6] B. Chen, S.K. Moon, X. Yao, G. Bi, J. Shen, J. Umeda, Strength and strain hardening of a selective laser melted AlSi10Mg alloy, Scr. Mater. 141 (2017) 45–49, https://doi.org/10.1016/j.scriptamat.2017.07.025.

[7] C. Galy, E.L. Guen, E. Lacoste, C. Arvieu, Main defects observed in aluminum alloy parts produced by SLM: from causes to consequences, Addit. Manuf. 22 (2018) 165–175, https://doi.org/10.1016/j.addma.2018.05.005.

[8] A. Raja, S.R. Cheethirala, P. Gupta, N.J. Vasa, R. Jayaganthan, A review on the fatigue behaviour of AlSi10Mg alloy fabricated using laser powder bed fusion technique, J. Mater. Res Technol. 17 (2022) 1013–1029, https://doi.org/10.1016/j.jmrt.2022.01.028.

[9] E. Brandl, U. Heckenberger, V. Holzinger, D. Buchbinder, Additive manufactured AlSi10Mg samples using selective laser melting (SLM): microstructure, high cycle fatigue, and fracture behavior, Mater. Des. 34 (2012) 159–169, https://doi.org/10.1016/j.matdes.2011.07.067.

[10] C. Zhang, H. Zhu, H. Liao, Y. Cheng, Z. Hu, X. Zeng, Effect of heat treatments on fatigue property of selective laser melting AlSi10Mg, Int J. Fatigue 116 (2018) 513–522, https://doi.org/10.1016/j.ijfatigue.2018.07.016.

[11] S. Bagherifard, N. Beretta, S. Monti, M. Riccio, M. Bandini, M. Guagliano, On the fatigue strength enhancement of additive manufactured AlSi10Mg parts by mechanical and thermal post-processing, Mater. Des. 145 (2018) 28–41, https://doi.org/10.1016/j.matdes.2018.02.055.

[12] E. Maleki, S. Bagherifard, O. Unal, M. Bandini, M. Guagliano, The effects of microstructural and chemical surface gradients on fatigue performance of laser powder bed fusion AlSi10Mg, Mater. Sci. Eng. A 840 (2022) 142962, https://doi.org/10.1016/j.msea.2022.142962.

[13] S. Beretta, S. Romano, A comparison of fatigue strength sensitivity to defects for materials manufactured by AM or traditional processes, Int J. Fatigue 94 (2017) 178–191, https://doi.org/10.1016/j.ijfatigue.2016.06.020.

[14] S. Romano, A. Abel, J. Gumpinger, A.D. Brandão, S. Beretta, Quality control of AlSi10Mg produced by SLM: metallography versus CT scans for critical defect size assessment, Addit. Manuf. 28 (2019) 394–405, https://doi.org/10.1016/j.addma.2019.05.017.

[15] C. Vargel. Corrosion of Aluminium, second ed., Elsevier Science, 2020 https://doi.org/10.1016/C2012-0-02741-X.

[16] C. Lin, S. Yang, Corrosion fatigue behavior of 7050 aluminum alloys in different tempers, Eng. Fract. Mech. 59 (6) (1998) 779–795, https://doi.org/10.1016/S0013-7944(97)00173-2.

[17] B.S. Gong, Z.J. Zhang, J.P. Hou, Q.Q. Duan, X.G. Wang, Z.F. Zhang, Effect of aging state on corrosion fatigue properties of 7075 aluminum alloy, Int J. Fatigue 161 (2022) 106916, https://doi.org/10.1016/j.ijfatigue.2022.106916.

[18] M.M. Sharma, J.D. Tomedi, J.M. Parks, A microscopic study on the corrosion fatigue of ultra-fine grained and conventional Al-Mg alloy, Corros. Sci. 93 (2015) 180–190, https://doi.org/10.1016/j.corsci.2015.01.020.

[19] Y. Wang, Y. Deng, J. Chen, Q. Dai, X. Guo, Effects of grain structure related precipitation on corrosion behavior and corrosion fatigue property of Al-Mg-Si alloy, J. Mater. Res Technol. 9 (3) (2020) 5391–5402, https://doi.org/10.1016/j.jmrt.2020.03.065.

[20] K. Chanyathunyaroj, S. Phetchcrai, G. Laungsopapun, A. Rengsomboon, Fatigue characteristics of 6061 aluminum alloy subject to 3.5% NaCl environment, Int J. Fatigue 133 (2020) 105420, https://doi.org/10.1016/j.ijfatigue.2019.105420.

[21] R.M. Chlistovsky, P.J. Heffernan, D.L. DuQuesnay, Corrosion-fatigue behaviour of 7075-T651 aluminum alloy subjected to periodic overloads, Int J. Fatigue 29 (2007) 1941–1949, https://doi.org/10.1016/j.ijfatigue.2007.01.010.

[22] Z. Ye, D. Liu, X. Zhang, X. Zhang, M. Lei, Z. Yang, Corrosion fatigue behavior of 7A85 aluminum alloy thick plate in NaCl solution, Acta Metall. Sin. (Engl. Lett. 28 (8) (2015) 1047–1054, https://doi.org/10.1007/s40195-015-0293-x.

[23] M. Guérin, J. Alexis, E. Andrieu, C. Blanc, G. Odemer, Corrosion-fatigue lifetime of aluminium-copper-lithium alloy 2050 in chloride solution, Mater. Des. 87 (2015) 681–692, https://doi.org/10.1016/j.matdes.2015.08.003.

[24] C. Rochet, M. Veron, E.F. Rauch, T.C. Lowe, B. Arfaei, A. Laurino, Influence of equal-channel angular pressing on the microstructure and corrosion behaviour of a 6xxx aluminium alloy for automotive conductors, Corros. Sci. 166 (2020) 108453, https://doi.org/10.1016/j.corsci.2020.108453.

[25] C. Rochet, E. Andrieu, B. Arfaei, J.P. Harouard, A. Laurino, T.C. Lowe, Influence of equal-channel angular pressing on the corrosion fatigue behaviour of an Al-Mg-Si aluminium alloy for automotive conductors, Int J. Fatigue 140 (2020) 105812, https://doi.org/10.1016/j.ijfatigue.2020.105812.

[26] A. Behvar, M. Haghshenas, A critical review on very high cycle corrosion fatigue: mechanisms, methods, materials, and models, J. Space Saf. Eng. 10 (2023) 284–323, https://doi.org/10.1016/j.jsse.2023.05.002.

[27] M. Cabrini, S. Lorenzi, T. Pastore, C. Testa, D. Manfredi, M. Lorusso, Corrosion behavior of AlSi10Mg alloy produced by laser powder bed fusion under chloride exposure, Corros. Sci. 152 (2019) 101–108, https://doi.org/10.1016/j.corsci.2019.03.010.

[28] Y. Zheng, Z. Zhao, R. Xiong, G. Ren, M. Yao, W. Liu, Effect of post heat treatment on microstructure, mechanical property and corrosion behavior of AlSi10Mg alloy fabricated by selective laser melting, Prog. Nat. Sci. 34 (2024) 89–101, https://doi.org/10.1016/j.pnsc.2024.02.001.

[29] A. Leon, E. Aghion, Effect of surface roughness on corrosion fatigue performance of AlSi10Mg alloy produced by selective laser melting (SLM), Mater. Charact. 131 (2017) 188–194, https://doi.org/10.1016/j.matchar.2017.06.029.

[30] C. Linder, F. Vucko, T. Ma, S. Proper, E. Dartfeldt, Corrosion-fatigue performance of 3D-printed (L-PBF) AlSi10Mg, Materials 16 (2023) 5964, https://doi.org/10.3390/ma16175964.

[31] ASTM F3318-18 Standard for Additive Manufacturing - Finished Part Properties - Specification for AlSi10Mg with Powder Bed Fusion-Laser Beam.

[32] ASTM E8/E8M-22. Standard Test Methods for Tension Testing of Metallic Materials.

[33] M. Yasuda, F. Weinberg, D. Tromans, Pitting corrosion of Al and Al-Cu single crystals, J. Electrochem Soc. 137 (1990) 3708–3715, https://doi.org/10.1149/1.2086291.

[34] U. Trdan, J. Grum, Evaluation of corrosion resistance of AA6082-T651 aluminium alloy after laser shock peening by means of cyclic polarisation and ElS method, Corros. Sci. 59 (2012) 324–333, https://doi.org/10.1016/j.corsci.2012.03.019.

[35] M. Trueba, S.P. Trasatti, Study of Al alloy corrosion in neutral NaCl by the pitting scan technique, Mater. Chem. Phy 121 (2010) 523–533, https://doi.org/10.1016/j.matchemphys.2010.02.022.

[36] ISO 12107:2012(E). Metallic materials-Fatigue testing-Statistical planning and analysis of data.

[37] Y. Kondo, Prediction of fatigue crack initiation life based on pit growth, Corrosion 45 (1989) 7–11, https://doi.org/10.5006/1.3577891.

[38] S.I. Rokhlin, J.Y. Kim, H. Nagy, B. Zoofan, Effect of pitting corrosion on fatigue crack initiation and fatigue life, Eng. Fract. Mech. 62 (1999) 425–444, https://doi.org/10.1016/S0013-7944(98)00101-5.

[39] G.S. Chen, K.C. Wan, M. Gao, R.P. Wei, T.H. Flournoy, Transition from pitting to fatigue crack growth-modeling of corrosion fatigue crack nucleation in a 2024-T3 aluminum alloy, Mater. Sci. Eng. A 219 (1996) 126–132, https://doi.org/10.1016/S0921-5093(96)10414-7.

[40] M. Tiryakioglu, On the size distribution of fracture-initiating defects in Al- and Mg-alloy castings, Mater. Sci. Eng. A 476 (2008) 174–177, https://doi.org/10.1016/j.msea.2007.04.088.

[41] M. Tiryakioglu, Relationship between defect size and fatigue life distributions in Al-7 Pct Si-Mg alloy castings, Met. Mater. Trans. A 40 (2009) 1623–1630, https://doi.org/10.1007/s11661-009-9847-8.

[42] H. Chen, X. Wang, X. Ren, Size effect on fatigue performance of SLM-ed AlSi10Mg alloy: role of defect size distribution, Int J. Fatigue 182 (2024) 108163, https://doi.org/10.1016/j.ijfatigue.2024.108163.

[43] M. Shirani, G. Härkegård, Large scale axial fatigue testing of ductile cast iron for heavy section wind turbine components, Eng. Fail Anal. 18 (2011) 1496–1510, https://doi.org/10.1016/j.engfailanal.2011.05.005.

[44] M. Shirani, G. Härkegård, Fatigue life distribution and size effect in ductile cast iron for wind turbine components, Eng. Fail Anal. 18 (2011) 12–24, https://doi.org/10.1016/j.engfailanal.2010.07.001.

[45] Y. Murakami, M. Endo. Effects of hardness and crack geometries on ΔKth of small cracks emanating from small defects. The Behaviour of Short Fatigue Cracks, EGF Pub. 1 (Edited by K.J. Miller, E.R. de los Rios) Mech. Eng. Publ. London, 1986; pp. 275-293. https://doi.org/10.2472/jsms.35.911.

[46] Y. Murakami. Metal Fatigue: Effects of Small Defects and Nonmetallic Inclusions, second ed, Elsevier: Academic Press, 2019, https://doi.org/10.1016/C2016-0-05272-5.

[47] X. Cao, W. Wallace, J.P. Immarigeon, C. Poon, Research and progress in laser welding of wrought aluminum alloys. II. Metallurgical microstructures, defects and mechanical properties, Mater. Manuf. Process 18 (2003) 23–49, https://doi.org/10.1081/amp-120017587.

[48] E.O. Olakanmi, R.F. Cochrane, K.W. Dalgarno, A review on selective laser sintering/melting (SLS/SLM) of aluminium alloy powders: processing, microstructure, and properties, Prog. Mater. Sci. 74 (2015) 401–477, https://doi.org/10.1016/j.pmatsci.2015.03.002.